
ORIGINAL ARTICLE

Journal Section

Statistical and Topological Summaries Aid Disease Detection for Segmented Retinal Vascular Images

John T. Nardini¹ | Charles W.J. Pugh² | Helen M. Byrne²

¹Department of Mathematics and Statistics,
The College of New Jersey, Ewing, NJ,
08628, USA

²Mathematical Institute, University of
Oxford, Oxford, Oxfordshire, OX2 6GG,
United Kingdom

³Ludwig Institute for Cancer Research,
Nuffield Department of Medicine,
University of Oxford, Oxford, Oxfordshire,
OX3 7DQ, United Kingdom

Correspondence

John T. Nardini PhD, Department of
Mathematics and Statistics, The College of
New Jersey, Ewing, NJ, 08628, USA
Email: nardinij@tcnj.edu

Funding information

HMB is grateful for the support provided by
the UK Centre for Topological Data
Analysis EPSRC grant EP/R018472/1.

Disease complications can alter vascular network morphology and disrupt tissue functioning. Diabetic retinopathy, for example, is a complication of type 1 and 2 diabetes mellitus that can cause blindness. Microvascular diseases are assessed by visual inspection of retinal images, but this can be challenging when diseases exhibit silent symptoms or patients cannot attend in-person meetings. We examine the performance of machine learning algorithms in detecting microvascular disease when trained on either statistical or topological summaries of segmented retinal vascular images. We apply our methods to four publicly-available datasets and find that the fractal dimension performs best for high resolution images. By contrast, we find that topological descriptor vectors quantifying the number of loops in the data achieve the highest accuracy for low resolution images. Further analysis, using the topological approach, reveals that microvascular disease may alter morphology by reducing the number of loops in the retinal vasculature. Our work provides preliminary guidelines on which methods are most appropriate for assessing disease in high and low resolution images. In the longer term, these methods could be incorporated into automated disease assessment tools.

KEYWORDS

microvascular network morphology, segmented image quantification, topological data analysis, persistent homology, fractal analysis, machine learning, disease prediction.

1 | INTRODUCTION

Blood vessel networks deliver nutrients and remove waste to maintain tissue homeostasis [1]. Disease complications can alter vascular network morphology, which may lead to insufficient oxygen levels or waste buildup that disrupt tissue function [2, 3]. For example, type 1 and 2 diabetes mellitus (T1DM and T2DM) cause high blood sugar levels, which damage small retinal blood vessels and can lead to diabetic retinopathy (DR) [4, 5, 6]. DR is the leading cause of blindness in the United States for individuals between the ages of 20 and 64 [7, 8]. Due to the high prevalence of T1DM and T2DM worldwide, DR incidence is expected to increase over the next 20 years [9].

To prevent DR, the United States and United Kingdom recommend that patients diagnosed with T1DM or T2DM attend annual eye exams. During these exams, physicians image patients' retinas using fundus photography. The image is then visually inspected for signs of DR, which include leaking blood vessels, edema, capillary non-perfusion, and damaged nerve tissue [2, 10]. In extreme cases, more advanced imaging techniques can be used to provide a more detailed view of the retinal vasculature. While these examinations are effective in preventing DR severity, DR incidence is still projected to increase due to patients exhibiting silent DR symptoms, low exam compliance, and a lack of patient access to health care [9, 11]. There is thus a growing need for the development of widely-accessible screening tools that are capable of detecting early signs of DR as a means to reduce its economic and healthcare impact on the global population.

Computational methods that quantify vascular morphology present a promising tool to aid microvascular disease detection. Many metrics summarizing static vascular features have been proposed to aid microvascular disease detection, including artery and vessel diameter ratios, tortuosity, and average daughter vessel branching angle, among others [2]. The fractal dimension (Df) descriptor is now commonly used to quantify network complexity, and Popovic et al. showed that Df increases with DR severity on the Standard Diabetic Retinopathy

Database Calibration Level 1 dataset [12, 13]. The effectiveness of the Df descriptor for DR detection is limited, however, as in this study it was only applied to images of retinal vascular networks with many branches. There is no consensus about the relationship between Df and DR; other studies have reported Df increases [14, 15] and decreases [16, 17, 18] with increasing DR severity.

Topological data analysis (TDA) provides an alternative computational method to aid disease detection. TDA is a recent field of mathematics that uses concepts from topology and geometry to infer the structure of data [19, 20]. Persistent homology (PH) is a commonly-used area of TDA that identifies topological features (e.g., connected components and loops) that are characteristic of a dataset [21]. As opposed to scalar-valued summary statistics, PH produces vectors that summarize features in the data across multiple scales. Additionally, previous theoretical results guarantee that PH computations are robust when data is noisy or incomplete [22].

TDA summaries have been used to detect disease from medical data, with applications in melanoma [23], breast cancer [24], pulmonary disease [25], heart disease [26], and Covid-19 [27, 28]. Several of these studies combine TDA summaries with machine learning algorithms to cluster, or classify, the data into groups that share similar topological characteristics and disease status [26, 27, 29]. Disease prediction is then performed by computing the same topological summaries on unseen data and identifying the cluster to which each dataset belongs.

Thus, TDA, and in particular PH, computations represent a promising multiscale approach to describe vascular network morphology, which may aid microvascular disease detection. PH has been applied to vascular network data previously: Bendich et al. showcased how PH summaries can reveal the effects of aging on brain vascular morphology [30], and Stolz et al. used PH to uncover effects of radiotherapy on tumor vascular structure not seen using statistical methods [31]. We recently applied PH computations and a machine learning algorithm to cluster a large collection of simulated vessel networks according to their topological features [32]. We found

that simulations within the same clusters were generated from similar input model parameters.

We propose that both statistical and PH computations of segmented retinal vascular network images, can be combined with machine learning algorithms to detect disease in medical images. While we focus on segmented vascular images, Garside et al. combined PH computations of colored fundus images with machine learning to detect DR [33]. Their work was applied to high resolution images, and the prediction algorithms required many input summaries to achieve high accuracy levels. We apply our methods to low and high resolution images and are able to achieve similar accuracy levels with only one statistical or topological summary.

In this work, we show that both statistical and topological computations provide summaries that can aid microvascular disease detection from segmented vascular images. We apply these methods to four existing and publicly-available datasets, namely the STructured Analysis of the REtina (STARE) [34], Digital Retinal Images for Vessel Extraction (DRIVE) [35], Child Heart And health Study in England (CHASE) [36], and High Resolution Fundus (HRF) [37] datasets. Each dataset provides two-dimensional binary image segmentations that were manually annotated by experts from fundus images and a disease classification for each image. We train support vector machines to predict disease classification from either statistical or topological computations and use 5-fold cross validation to estimate the accuracy of each approach. We find that these methods achieve high accuracy levels when using statistical summaries of high resolution images and topological summaries of low resolution images. This work may provide guidelines for which computational methods are most suitable for microvascular disease analysis based on the quality of data. These guidelines can be used to develop automated medical tools to aid clinical decisions, which may make healthcare more effective, accessible, and affordable.

2 | MATERIALS AND METHODS

We obtained two-dimensional binary vessel segmentation images (VSIs) and their disease classifications from four publicly available datasets. We summarize the morphology of each VSI by computing standard descriptor vectors and topological descriptor vectors. These vectors are used to train a machine learning algorithm that predicts VSI disease classification. By comparing the algorithm's accuracy when trained with each input vector type, we identify descriptor vectors are most informative for disease prediction. The study pipeline is summarized in Figure 1 and consists of three steps: 1. data collection, 2. data analysis, and 3. disease prediction.

2.1 | Data collection

VSIs and their disease classifications were obtained the STARE, DRIVE, CHASE, and HRF datasets. Each VSI has been manually annotated from fundus images by expert inspection. VSIs are two-dimensional binary images, in which pixel values of one denote the presence of vasculature and pixel values of zero denote the absence of vasculature. The technical aspects of each dataset are summarized in Table 1.

The STARE dataset:

This dataset contains fundus images from 20 patients [34]. Each image was annotated separately by two experts, and has resolution 700×605 pixels. Of the 20 patients, 10 were diagnosed as 'Normal', and 10 were diagnosed with a specific disease, such as Hollenhorst emboli and vein occlusion. For simplicity, we classify the latter patients as 'Diseased'. The STARE data are available at <https://cecac.clemson.edu/~ahoover/stare/>.

The DRIVE dataset:

This dataset includes fundus images from 20 patients [35]. Each image was annotated once and has resolution 565×584 pixels. Of the 20 patients, 17 were diagnosed as Normal and 3 as Diseased. The DRIVE data are available at <https://drive.grand-challenge.org/>.

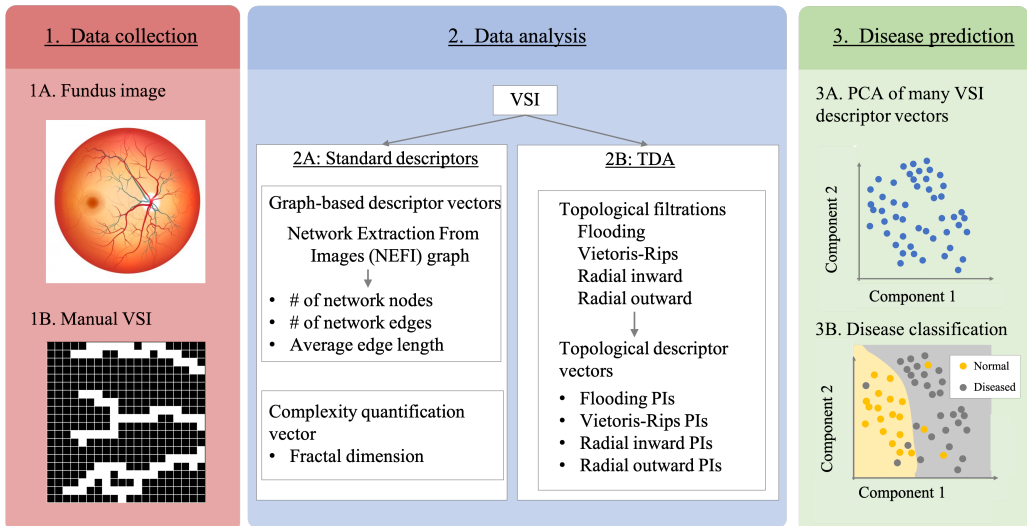


FIGURE 1 Methods pipeline overview. **1. Data collection.** Two-dimensional fundus images, their corresponding binary vessel segmentation images (VSIs), and their disease classifications were collected from four publicly available datasets. **2. Data analysis.** We compute standard descriptor vectors and topological descriptor vectors for each VSI. **A) Standard descriptors.** We compute standard descriptor vectors by first representing each VSI as a graph. We then count the number of nodes and edges in the graph, and compute its average edge length. We also quantify vessel network complexity by computing the fractal dimension for each VSI. **B) Topological data analysis (TDA).** We construct flooding, Vietoris-Rips, radial inward, and radial outward filtrations for each VSI. Each filtration yields two two-dimensional persistence images (PIs) that describe the connected components and loops of the filtration. The PIs are then vectorized. **3. Disease prediction.** VSI disease classification is predicted using either a standard descriptor vector or a vectorized PI from Step 2. **A) Principal components analysis (PCA)** is used to project vectorized PIs to their two dominant principal components. **B) Support vector machines** are trained to predict VSI disease classification using either dimension-reduced PIs or standard descriptor vectors.

TABLE 1 List of datasets used throughout the study.

	STARE	DRIVE	CHASE	HRF	All
Number of patients	20	20	14	45	n/a
VSI per patient	2	1	4	1	n/a
Total number of VSIs	40	20	56	45	161
Disease classes	Normal ($n = 20$),	Normal ($n = 18$)	n/a	Normal ($n = 15$)	Normal ($n = 109$)
	Diseased ($n = 20$)	Diseased ($n = 2$)		Diseased ($n = 30$)	Diseased ($n = 52$)

STARE, STructured Analysis of the REtina; DRIVE, Digital Retinal Images for Vessel Extraction; CHASE, Child Heart and Health Study in England; HRF, High Resolution Fundus; DR, Diabetic Retinopathy; VSI, Vessel segmentation image.

The CHASE dataset:

This dataset contains fundus images from the left and right retinas of 14 school children [36]. Each image was annotated separately by two experts, and has resolution 999×960 pixels. No diagnoses were made, so we classify all children as Normal. The CHASE data are available at <https://blogs.kingston.ac.uk/retinal/chasedb1/>.

The HRF dataset:

This dataset includes fundus images from 45 patients [37]. Each image was annotated once and has resolution $3,304 \times 2,336$ pixels. Of the patients, 15 were diagnosed as Normal, and 30 were diagnosed as diseased. The HRF data are available at <https://www5.cs.fau.de/research/data/fundus-images/>.

The All dataset:

We do not perform disease prediction on the DRIVE or CHASE datasets since they contain few Diseased images. Instead, we combine the VSIs from all four datasets into an "All" dataset that contains 161 VSIs where 109 are diagnosed as Normal and 52 as Diseased. We downsampled all VSIs to have the same resolution of 523×356 pixels.

2.2 | Data Analysis

2.2.1 | Standard descriptors

We summarise VSIs by computing three graph-based and one complexity vectors and refer to them collec-

tively as *standard descriptor vectors*.

In order to compute the standard descriptor vectors, we first use the Network Extraction From Images (NEFI) software to generate a graph for each VSI [38]. As shown in Figure 2, we place nodes at locations where three vessel segments intersect and also at terminal points of vessel segments. Edges connect pairs of nodes that are connected by a vessel segment in the VSI. We use the resulting graph to compute the following three network quantities: the number of nodes, the number of edges, and the average length of each edge.

We compute the fractal dimension (Df) of each VSI using the box-counting method [12]. This method decomposes the VSI into boxes of pre-determined side lengths. We consider ten box side lengths, s : for the largest value of s , four boxes cover the entire VSI; for the smallest value, each box is the size of one pixel. For each value of s , boxes are assigned a value of one if they contain at least one nonzero pixel; otherwise they are assigned a value of zero. We denote by $N(s)$ the number of boxes of size s and value one. We assume that $\ln(N(s))$ is linearly proportional to $\ln(1/s)$, in which case the slope of the line of best fit approximates the Df of a given VSI [39].

2.2.2 | Topological data analysis

TDA is an emerging field of research that combines concepts from algebraic topology and computational geometry to analyze the shape of high dimensional data. PH is a widely-used methodology within TDA [19, 21, 20]. In contrast to descriptors that summarize data at a sin-

NEFI-generated VSI graph representation

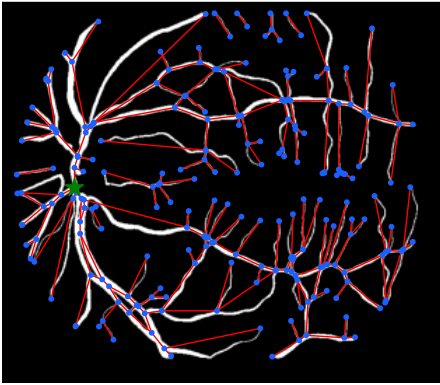


FIGURE 2 Example graph representation of a vessel segmentation image (VSI). A graph generated with the Network extraction from images (NEFI) software superimposed over the input VSI from the STARE dataset. Graph nodes are depicted by blue dots, graph edges are depicted by red lines, and the graph's central node is depicted by the green star. For this VSI, the computed standard descriptor values are: # nodes = 224, # edges = 234, Avg. edge length = 38.38 pixel lengths, and fractal dimension = 1.64.

gle scale, PH analyzes features of the data over many scales by varying a specific scale parameter (for VSIs, suitable parameters might include distance from a vessel segment or distance from the optic disk).

PH achieves a multiscale description of data through the construction of *filtrations*. From a range of scale parameter values, a filtration generates a sequence of embedded graph-like structures on the data points. Such structures are sparsely connected for small parameter values and highly connected for large parameter values. PH quantifies topological features in the filtration. The topological features we consider are connected components and loops (connections between data points enclosing an empty region). Features that are present across a large range of scale parameter values are called *persistent* and may be characteristic of a dataset. The output from PH are barcodes and persistence diagrams, which visualize the existence and persistence of topological features in the data. In order to compare PH outputs, perform statistical analyses, and/or apply classification methods from machine learning, persistence diagrams can be transformed (via persistence diagrams) into two-dimensional persistent images and their vectorizations [40].

We investigate how disease alters retinal morphology by computing four PH filtrations for each VSI: the Vietoris-Rips, flooding, radial outward, and radial inward filtrations. Before describing each filtration, we present an illustrative example that highlights the key concepts of PH.

Persistent Homology: an illustrative example

We now present an illustrative example of our PH pipeline (Figure 3), in which we apply the flooding filtration to the VSI from step 1B of Figure 1.

In part 1, we compute the flooding filtration by constructing a sequence of two-dimensional binary images. The first binary image identifies the vessel segments present in the VSI as white pixels, the second identifies the original vessel segments and their nearest neighbors as white pixels, the third identifies the original segments, their nearest neighbors and second nearest neighbors as white pixels, and so on. The process terminates when

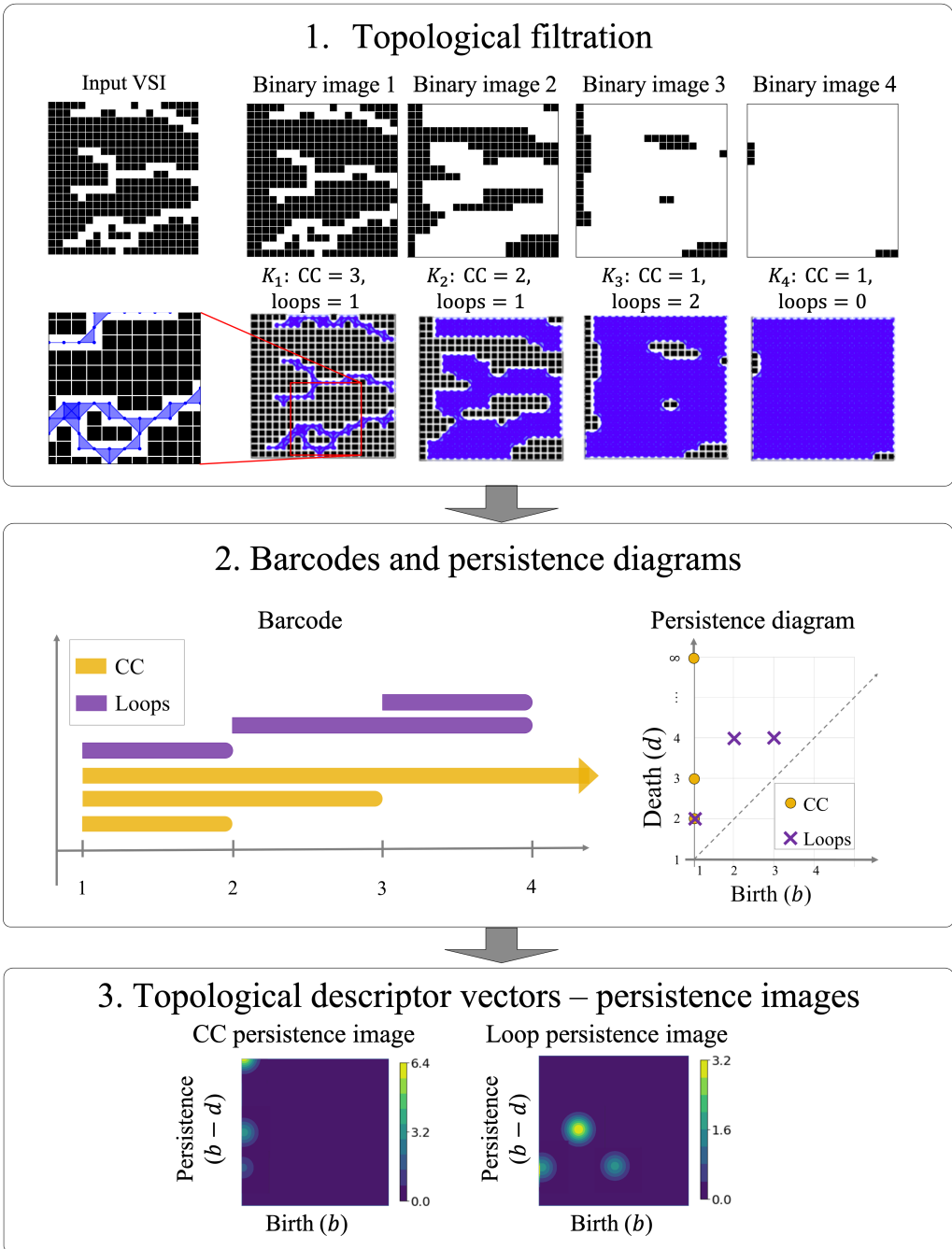


FIGURE 3 Persistent homology (PH) pipeline to quantify vessel segmentation image (VSI) morphology. The flooding filtration is applied to the VSI from step 1B of Figure 1. 1) Topological filtration. A sequence of binary images is constructed by applying a flooding step to the previous image, and starting with the initial image. Each binary image is then converted into a simplicial complex, K_i for $i = 1, 2, 3, 4$. PH quantifies the presence of connected components (CC) and loops within the filtration $\mathcal{K} = \{K_1, K_2, K_3, K_4\}$. 2) Barcodes and persistence diagrams. The lifetime of each topological feature type is summarized by a barcode or persistence diagram. 3) Topological descriptor vectors – Persistence images. Persistence diagrams are converted into persistence images, a form of topological descriptor vector that is suitable for machine learning tasks.

all pixels are white (for the VSI in Figure 3, this corresponds to binary image 5, not shown). We apply four flooding steps in this example, but typically more steps are needed to analyze real VSIs.

The sequence of binary images is then converted into a filtration by replacing each binary image with a set of points, lines and triangles, known collectively as a *simplicial complex*. The i^{th} ($i = 1, 2, 3, 4$) simplicial complex, K_i , is generated from the i^{th} binary image by placing a point at the centroid of each white pixel, drawing lines between any two neighboring points, and putting filled in triangles between any three neighboring points that form a right triangle (see zoomed-in inset of K_1 in Figure 3). The filtration is given by $\mathcal{K} = \{K_1, K_2, K_3, K_4\}$.

We use PH to quantify the lifetime, or persistence, of topological features (connected components and loops) in \mathcal{K} . A feature is born in filtration step $b \geq 1$ if it first appears in K_b ; intuitively, the feature dies on filtration step $d > b$ if it is no longer present in K_i , $i \geq d$; its persistence is defined to be $d - b$. For example, in K_1 , there are three connected components and one loop; in K_2 , one connected component dies (because two previous connected components join together), one loop dies (because it becomes filled in), and a new loop is born; in K_3 , one connected component dies, and a new loop is born; finally, in K_4 , a single connected component persists, and both loops die. Any additional flooding steps result in a completely white binary image, whose simplicial complexes contain one connected component and no loops.

In part 2 of the PH pipeline, we summarize topological features' lifetimes using barcodes and persistence diagrams. Within a barcode, each feature is represented by a bar of length $d - b$ placed in the interval $[b, d)$. For the example in Figure 3, the barcode of connected components is given by $\{[1, 2), [1, 3), [1, \infty)\}$, and the barcode of loops is given by $\{[1, 2), [2, 4), [3, 4)\}$. *Persistence diagrams* are an alternative way to depict the topological features; each persistence interval $[b, d)$ is represented by a two-dimensional point with co-ordinates (b, d) .

In part 3, we convert persistence diagrams into two-dimensional *persistence images* (PIs). The birth-death co-

ordinates, (b, d) , of topological features are replaced by a two-dimensional Gaussian distribution, centered at $(b, b - d)$ with constant variance ($\sigma = 1.0$). PIs are created by multiplying each Gaussian distribution by its persistence, $b - d$, and then summing over all weighted distributions. The resulting function is then converted into a discretized image, with a fixed grid size. Persistence images for connected components and loops are created separately and can be vectorized to facilitate subsequent analyses and comparison of VSIs.

Topological filtrations

There is currently no consensus about which topological filtrations are best suited for determining how disease alters VSI morphology and, in turn, predicting the presence of disease from VSI data. To address this question, we consider four filtrations: the Flooding filtration, the Vietoris-Rips filtration, and the radial outward and radial inward filtrations (Figure 4).

For each filtration, we define N values of its scale parameter; from the i^{th} ($i = 1, \dots, N$) value, we build a simplicial complex, K_i . A simplicial complex is a structure consisting of points, lines, triangles, and their higher-order counterparts that connect data points together. We refer to the resulting sequence of simplicial complexes,

$$\mathcal{K} = \{K_1, K_2, \dots, K_N\}, \quad (1)$$

as a filtration.

The Flooding filtration: We generate a sequence of two-dimensional binary images, starting with the original VSI (Figure 4, top row). We create a new binary image by looping over all nonzero pixels in the previous binary image. In addition to holding fixed the values of all nonzero pixels, we manually set to one the values of their eight neighboring pixels. This process is repeated until a sequence of 70 binary images have been generated, which completely fills in each VSI. We retain the odd-numbered images (resulting in a final sequence of 35 images) to ease subsequent computation.

We convert the i^{th} binary image into the simplicial complex, K_i^{flood} ($i = 1, 2, \dots, 35$), by placing points at

the centroids of all nonzero pixels, lines connecting any two points that are within the eight surrounding pixels of each other, and filled-in triangles connecting three neighboring points that form a right triangle.

The Vietoris-Rips filtration: We convert each VSI into a two-dimensional point cloud by placing a point at the centroid of each nonzero pixel (Figure 4, middle row). For computational reasons, we subsample 2000 representative points from the resulting point cloud data (i.e., approximately 10% of the points) using a Greedy furthest point sampling algorithm [41].

To construct the Vietoris-Rips filtration, \mathcal{K}^{VR} , we define $N = 40$ distance values $0 \leq \epsilon_1 < \epsilon_2 < \dots < \epsilon_N$ and place a circle of radius ϵ_i around each subsampled point. We connect, with a line, any two points whose circles overlap, and connect with a filled-in triangle any three points whose circles pairwise overlap. Each $\mathcal{K}_i^{\text{VR}}$ ($i = 1, 2, \dots, N$) is generated by combining all such points, lines, and filled-in triangles that result from ϵ_i . We choose $\epsilon_i = (i - 1)185/39$ to analyze each dataset.

The radial outward and inward filtrations: We consider a radial outward filtration, $\mathcal{K}^{\text{outward}}$, and a radial inward filtration, $\mathcal{K}^{\text{inward}}$ (the radial outward filtration is depicted in Figure 4, bottom row). In both cases, for a given VSI, we first compute a graph that comprises a set of nodes, V , and a set of edges, E (Figure 2). Each node is placed at locations where three vessel segments intersect and also at terminal points of vessel segments. Edges connect pairs of nodes that are connected by a vessel segment in the VSI. We use the NEFI software to generate each graph [38]. We designate the node from V with the smallest betweenness centrality measure as the graph's central node, v^c (see green star in Figure 2). This definition for v^c was chosen to identify a node located near the optic disk of each VSI.

To construct $\mathcal{K}^{\text{outward}} = \{\mathcal{K}_1^{\text{outward}}, \dots, \mathcal{K}_{40}^{\text{outward}}\}$, we consider $N = 40$ radial values $0 \leq r_1 < r_2 < \dots < r_{40}$. All nodes from V located within distance r_i of v^c are included as points in $\mathcal{K}_i^{\text{outward}}$. If two nodes included in $\mathcal{K}_i^{\text{outward}}$ are connected by an edge from E , then we connect them with a line in $\mathcal{K}_i^{\text{outward}}$. We do not include filled-in triangles in $\mathcal{K}_i^{\text{outward}}$. For the HRF dataset, we choose $r_i = (i - 1)3000/39$ pixel lengths; for all other

datasets, we choose $r_i = (i - 1)700/39$ pixel lengths. These values ensure that all computed NEFI graphs are covered by the end of the filtration.

To construct $\mathcal{K}^{\text{inward}} = \{\mathcal{K}_1^{\text{inward}}, \dots, \mathcal{K}_N^{\text{inward}}\}$, we use the same radial values r_i ($i = 1, 2, \dots, N$) as those used for the radial outward filtration, and proceed as follows. All nodes from V located at a distance $r_N - r_i$, or greater, from v^c are included as points in $\mathcal{K}_i^{\text{inward}}$. If two nodes included in $\mathcal{K}_i^{\text{inward}}$ are connected by an edge in E , then we connect them with a line in $\mathcal{K}_i^{\text{inward}}$. We do not include filled-in triangles in $\mathcal{K}_i^{\text{inward}}$.

Barcodes and Persistence diagrams

PH quantifies the lifetimes of topological features, here connected components and loops, in a filtration using barcodes and persistence diagrams [19, 20, 21, 42, 43]. As discussed in the illustrative example, a barcode is a collection of intervals $\{[b_1, d_1], \dots, [b_k, d_k]\}$ designating the birth and death times of each topological feature, and a persistence diagram is a collection of two-dimensional points $\{(b_1, d_1), \dots, (b_k, d_k)\}$ summarizing the lifetime of each topological feature (Figure 3). We create two separate persistence diagrams from each filtration, one for connected components and one for loops. We use Ripser (version 0.4.1) to perform PH for the Vietoris-Rips filtration and Gudhi (version 3.4.1) for the remaining filtrations.

Persistence images

We require vectors of the same length to represent each VSI for disease prediction. Therefore, we map all persistence diagrams into two-dimensional *persistence images* (PIs) of the same size and convert the PIs into vectors of a fixed length (Figure 3). The resulting topological descriptor vectors are stable to perturbations in data and can be used for machine learning and data science algorithms [20, 32, 40].

Briefly, a PI is computed from a persistence diagram in the following way:

1. Each birth-death pair (b, d) is transformed to a birth-persistence pair $(b, p) = (b, d - b)$;
2. Each (b, p) pair is recast as a two-dimensional Gaus-

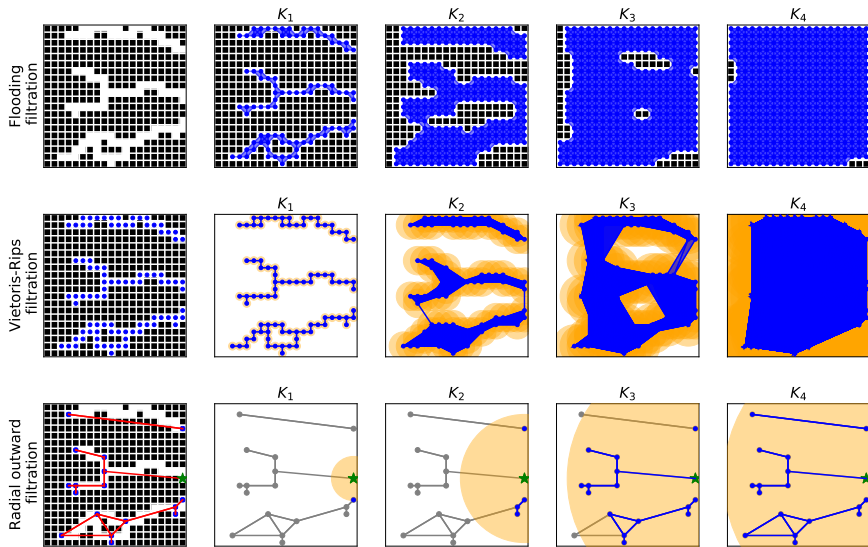


FIGURE 4 Overview of topological filtrations. (Top row) The Flooding filtration creates a sequence of simplicial complexes from a sequence of binary images. (Middle row) The Vietoris-Rips filtration creates a sequence of simplicial complexes from a point cloud by connecting together points that are within a given radius of each other. (Bottom row) The Radial outward filtration creates a sequence of simplicial complexes from a graph by including nodes within a given radius of the graph's central node (denoted with a green star). The radial inward filtration is not shown.

- sian normal distribution, with mean (b, ρ) and variance σ (here, we fix $\sigma = 1.0$);
3. Each Gaussian is discretized to produce a two-dimensional image of size $N_{PI} \times N_{PI}$ (here, we fix $N_{PI} = 50$);
 4. All Gaussian images are multiplied by their persistence, ρ , and then summed to produce the PI;
 5. The PI is vectorized into a $N_{PI}^2 \times 1$ topological descriptor vector for disease prediction.

More information on PIs and their computation is available in [40]. We compute separate PIs for connected components and loops from each filtration, producing 8 total topological descriptor vectors for each VSI.

2.2.3 | Data prediction

Dimensionality reduction

Each vectorized PI is of length 2,500 because we fix $N_{PI} = 50$. We use principal components analysis (PCA), to reduce each vectorized PI into a length 2 vector (See Step 3A of Figure 1) and facilitate data analysis. The PCA algorithm maximizes the amount of information (*i.e.*, statistical variability) present in the reduced data. We use Sci-kit learn's decomposition package (version 0.24.2) to perform PCA.

Disease classification

For each descriptor vector, we use a supervised learning algorithm to predict VSI disease classification. In more detail, we implement support vector machines (SVMs), with radial basis function kernels, to identify the curves or surfaces that best partition the data into distinct groups according to disease type (See Step 3B in Figure 1). We use Sci-kit learn's svm package for SVM implementation.

We perform 5-fold cross validation to quantify and then compare the accuracy of SVMs associated with each of the standard and topological descriptor vectors. Given M data-classification points $(\mathbf{x}_1, y_1), (\mathbf{x}_2, y_2), \dots, (\mathbf{x}_M, y_M)$, where \mathbf{x}_i is a descriptor vector and y_i is the corresponding disease classification ($y_i = 0$ for Normal, $y_i = 1$ for Diseased), cross valida-

tion is performed as follows. During a given round of cross validation, 80% of the data-classification points are placed into a training dataset and the remaining 20% are placed into a testing dataset. An SVM, trained with the training dataset to predict y_i from \mathbf{x}_i , is then used to predict the classification of each \mathbf{x}_i from the testing dataset. The SVM's out-of-sample (OOS) accuracy is the percentage of these predictions that match the true classification labels. In 5-fold cross validation, the mean OOS accuracy of the SVM is determined from five different training-testing splits, and each data-classification pair is placed in the testing dataset only once. Since the OOS accuracy score depends on how the data are split, we perform 100 rounds of 5-fold cross validation and report average values and their standard deviations.

3 | RESULTS

3.1 | Fractal dimension is the most accurate standard descriptor of disease

We predicted VSI disease classifications using SVMs associated with each standard descriptor vector for the STARE, HRF, and All datasets (Table 2). We treated the two STARE experts' annotated VSI collections as separate datasets. SVMs associated with the Df vector usually outperformed the other standard descriptors, achieving the highest OOS accuracy for the STARE and HRF datasets, although the average edge length vector performed best on the All dataset. A histogram of the Df values for the HRF dataset shows that this descriptor partitions the dataset into two distinct groups representing Normal and Diseased VSIs (Figure 5).

The computed mean Df values decrease in the presence of disease for the STARE and HRF datasets but increase in the presence of disease on the All dataset (Table 3). On the STARE and HRF datasets, the mean Df values for normal and diseased VSIs vary, but the relative percentage reductions (3.1%, 5.2%, and 2.7% for STARE expert 1, STARE expert 2 and HRF datasets, respectively) are similar in magnitude. We conclude that, for the retinal diseases contained within the datasets, the associated vascular networks are less complex than

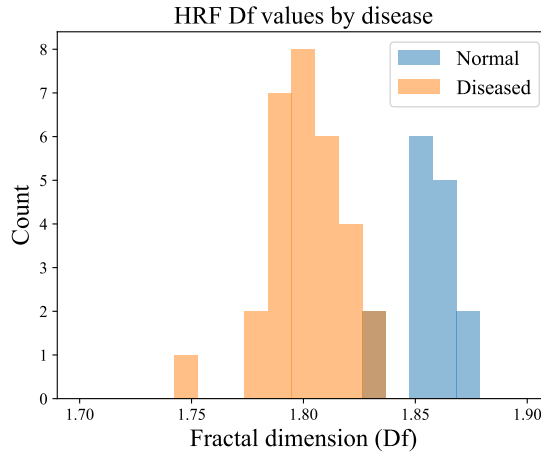


FIGURE 5 Histogram summarizing the computed values of the fractal dimension, Df, for Normal and Diseased vessel segmentation images (VSIs) from the HRF dataset.

TABLE 2 Summary of the mean out-of-sample (OOS) accuracy scores (standard deviations in parentheses) obtained when standard descriptor vectors are used to train support vector machines (SVMs) to predict the disease status of VSIs from all four datasets. Bold highlights the highest OOS accuracy for a given dataset. Rows are ordered by vectors with the highest mean OOS accuracy score across all four datasets.

Standard Descriptors	STARE expert 1	STARE expert 2	HRF	All
Df	81 (3.8) %	85 (4.3) %	95 (1.4) %	63 (1.7) %
Avg. Edge length	59 (6.1) %	51 (7.6) %	69 (2.2) %	76 (1.2) %
# Nodes	54 (5.7) %	50 (6.5) %	70 (2.1) %	69 (1.4) %
# Edges	51 (5.6) %	50 (6.0) %	69 (2.6) %	64 (1.6) %

Df, fractal dimension; Avg., average.

those for healthy retinas. On the All dataset, the mean Df value increased by 1.8% in the presence of disease. The discrepancy between these results may be an artifact of the data: over half of the Diseased images in the All dataset are from the HRF dataset (which has more complex VSIs) while over half of the Normal images are from the STARE, DRIVE, and CHASE datasets (which have simpler VSIs).

3.2 | Topological descriptor vectors accurately predict disease classification

We used SVMs associated with each topological descriptor vector to predict VSI disease classifications for all

datasets (Table 4). On the STARE datasets, SVMs associated with flooding (loops) PIs perform best or second-best and outperform the Df descriptor vector. The SVM trained on the Vietoris-Rips (loops) PIs perform best on the HRF dataset. On the All dataset, the SVM associated with the Vietoris-Rips (connected components) PI performs best, though the flooding (loops) and Vietoris-Rips (loops) PIs also perform well.

3.3 | Interpretation of the topological descriptor vectors

Plotting the dimension-reduced flooding (loops) PIs from the STARE expert 1 dataset onto their first two

TABLE 3 Average fractal dimension (Df) values for Normal and Diseased VSIs from all four datasets.

	STARE expert 1	STARE expert 2	HRF	All
Mean Normal Df value (standard deviation)	1.63 (0.015)	1.72 (0.014)	1.85 (0.011)	1.65 (0.066)
Mean Diseased Df value (standard deviation)	1.58 (0.036)	1.63 (0.058)	1.80 (0.016)	1.68 (0.051)

TABLE 4 Summary of the mean out-of-sample (OOS) accuracy scores (standard deviations in parentheses) obtained when topological descriptor vectors are used to train SVMs to predict the disease status of VSIs from all four datasets. Bold highlights the highest OOS accuracy for a given dataset and underlined values are within 5 percentage points of the highest score. Rows are ordered by vectors with the highest mean OOS accuracy score on all four datasets.

Standard Descriptors	STARE expert 1	STARE expert 2	HRF	All
VR (loops)	95 (1.6) %	82 (2.6) %	95 (1.6) %	<u>83 (0.9) %</u>
Flooding (loops)	<u>93 (3.2) %</u>	94 (3.9) %	60 (4.7) %	<u>84 (0.6) %</u>
VR (CC)	79 (3.1) %	78 (3.5) %	79 (3.1) %	87 (0.5) %
Radial out (loops)	84 (2.9) %	58 (7.8) %	80 (4.0) %	71 (1.6) %
Radial out (CC)	62 (7.6) %	45 (10.7) %	61 (3.9) %	81 (0.7) %
Radial in (CC)	36 (10.0) %	58 (9.7) %	63 (4.2) %	80 (0.8) %
Flooding (CC)	54 (7.0) %	37 (8.4) %	59 (4.1) %	77 (1.3) %
Radial in (loops)	38 (9.2) %	47 (6.9) %	64 (4.2) %	62 (2.4) %

CC, connected components.

principal components clearly partitions the Normal and Diseased data (Figure 6). Visual inspection of the VSI data reveals structural differences between the two groups: Normal VSIs exhibit highly-branched and intertwined vessel networks, whereas Diseased VSIs contain fewer secondary branches and form loosely-connected vessel networks. The flooding (loops) PIs are able to summarize these dominant (topological) features. A representative PI from a Normal patient has a high PI density along the vertical line $b = 0$, indicating that many loops are present in the VSI. A representative Diseased PI has smaller densities along this line because it has fewer loops. We observe similar results when the dimension-reduced flooding (loops) PIs from the STARE expert 2 dataset are projected onto their first two principal components (Supplementary Figure 1).

SVMs trained on the dimension-reduced Vietoris-Rips (loops) PIs achieve the highest mean OOS accuracy scores on the HRF dataset. Projecting these PIs onto their first two principal components partitions the Normal and Diseased Data (Supplementary Figure 1). In these data, Normal VSIs exhibit more branched net-

works than Diseased VSIs. One consequence of this morphological difference is that the Normal PIs have higher densities near the horizontal line $\rho = 0$. The increased density of the Normal PIs suggests that, for Normal VSIs, more transient loops form during the Vietoris-Rips filtration than for the Diseased VSIs.

4 | DISCUSSION

We studied the accuracy of machine learning classifiers in predicting VSI disease status when trained with either standard descriptor vectors or topological descriptor vectors. The classifiers achieved the highest predictive accuracy on the HRF dataset when trained with either the fractal dimension or Vietoris-Rips (loops) descriptors. On the STARE dataset, the flooding (loops) descriptor achieved the best results. Further analysis showed that, for the four datasets of interest, disease reduces VSI complexity, as quantified by fractal dimension. We also found that diseased VSIs have fewer loops, as quantified with the flooding and Vietoris-Rips filtra-

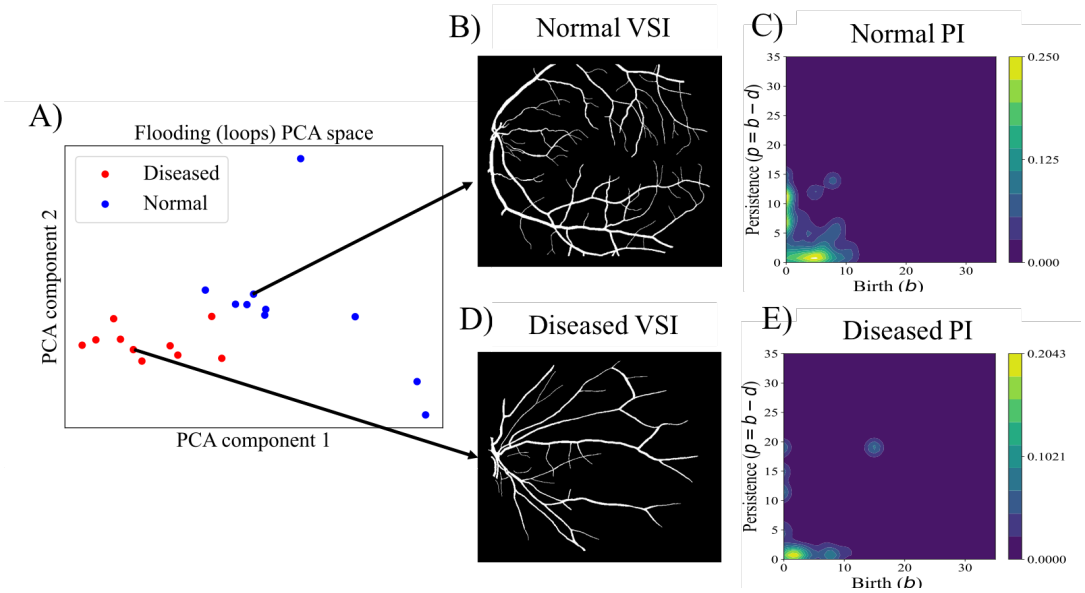


FIGURE 6 Flooding (loops) PIs partition the STARE expert 1 dataset. A) Plotting the dimension-reduced flooding (loops) PIs along the first two principal components. B) Representative Normal VSI, and C) Flooding (loops) PI from the representative Normal VSI. D) Representative Diseased VSI, and E) Flooding (loops) PI from the representative Diseased VSI.

tions. These findings point to morphological differences between Normal and Diseased VSIs in these datasets.

The results reported in this article suggest that the most informative metrics for diagnosing microvascular disease from VSIs are context specific; fractal dimension provides an accurate diagnostic feature for high resolution (but not low resolution) VSIs. Quantifying loops using the flooding filtration provides the most accurate diagnostic metric for disease classification of low resolution VSIs from the STARE dataset and also performed well on the All dataset. The Vietoris-Rips filtration also provides accurate disease classification metrics for the HRF dataset and All datasets.

In this study, we have shown how statistical and topological methods can aid assessment of microvascular disease. However, each of the top-performing methods has limitations, which suggests that more research is needed to determine which metrics (or combinations of metrics) should be used to analyse and classify VSIs. For example, the accuracy of the Vietoris-Rips (loops) topo-

logical descriptor changed by 13 percentage points between the two STARE datasets, even though these data were created from the same fundus images, from the same patients. While the fractal dimension performed consistently on both STARE datasets, it was less accurate than the Flooding (loops) descriptor. The Flooding (loops) descriptor did not perform well on the HRF dataset. A possible source of these limitations is the small size of the datasets. In the future, we aim to analyze larger datasets, including longitudinal data, to determine how descriptors change with disease progression and to identify methods that perform consistently and robustly across datasets. We aim also to create new descriptors that combine statistical and topological methods to improve the accuracy of disease assessment.

We combined statistical and topological methods with a machine learning algorithm to detect microvascular disease from VSIs. In separate work, Garside et al. [33] applied another TDA method to fundus images in order to detect diabetic retinopathy. Taken to-

gether, these studies provide preliminary evidence supporting the potential for combining methods from statistics and TDA with machine learning algorithms to automate detection of retinal diseases from medical images. A strength of TDA is that it is underpinned by mathematical theory, including stability results which guarantee that small changes to input data (e.g., the removal or addition of vessel segments) do not significantly alter the resulting output [22]. This stability result is illustrated by the good agreement between the output of the flooding filtration (loops) when applied to the two sets of annotations from the STARE dataset. In future work, we plan to implement extended persistence and multiparameter persistence to determine whether they provide more robust quantification of VSIs [44, 45].

We note that artificial neural networks are an alternative approach to automate the detection of microvascular disease [46]. Because deep neural networks perform exceptionally well on computer vision tasks, several recent studies have proposed their use to extract VSIs from fundus images and then use them to predict disease classification [47, 48, 49]. A concern about the use of neural networks, however, is that it can be challenging to interpret the outputs from these black-box models [50]. Topological and statistical analyses, on the other hand, generate metrics that are interpretable. In future work, we plan to combine topological and statistical methods with machine learning algorithms and mathematical modeling to infer the mechanisms that lead to diabetic retinopathy and other microvascular diseases of the retina [32, 51].

A limitation of this study is the small sample size. We focused on the STARE, DRIVE, CHASE, and HRF datasets due to their wide use in the scientific community and public availability. In the future, we aim to produce a fully automated pipeline that uses neural networks to extract VSIs from fundus images and then uses our methodology for their analysis and classification [52]. This will enable us to analyze larger retinal image datasets and to distinguish different disease types (e.g., Normal, diabetic retinopathy, or Glaucoma).

In this work, we focused on two-dimensional VSIs, but TDA methods have been used to characterize three-

dimensional vascular networks in the brain and in cancer [30, 31]. These methods could be adapted to analyze three-dimensional, optical coherence tomography angiography images [53].

5 | PERSPECTIVE

Our work shows how statistical and topological methods can be combined with machine learning algorithms to predict whether retinal vascular networks are Normal or Diseased. A statistical approach, in which the fractal dimension descriptor is used to quantify the vascular networks, provides the most accurate classification of high resolution images, while topological methods, involving a flooding filtration, excelled when analyzing low resolution images. Taken together, these results highlight the importance of testing a range of alternative metrics when designing automated tools to analyze, quantify and classify biomedical imaging data.

The methods developed in this work could also contribute to the growing use of telemedicine in making healthcare more accessible, affordable and effective. High resolution digital images of a patient's eyes, taken using smartphones, could be sent to clinics for automated analysis and disease classification, prior to review by a medical expert. In addition to delivering remote clinical services to patients, automated diagnoses prior to medical consultations, would enable doctors to devote more time to evaluating non-standard cases.

acknowledgements

The authors thank BJ Stolz for helpful discussion and commentary.

conflict of interest

The authors declare no conflicts of interest.

references

- [1] Davis GE, Norden PR, Bowers SLK. Molecular control of capillary morphogenesis and maturation by

- recognition and remodeling of the extracellular matrix: functional roles of endothelial cells and pericytes in health and disease. *Connective Tissue Research* 2015 Sep;56(5):392–402.
- [2] Kee AR, Wong TY, Li LJ. Retinal vascular imaging technology to monitor disease severity and complications in type 1 diabetes mellitus: A systematic review. *Microcirculation* 2017;24(2):e12327.
- [3] MacCormick IJC, Zheng Y, Czanner S, Zhao Y, Diggle PJ, Harding SP, et al. Spatial statistical modelling of capillary non-perfusion in the retina. *Scientific Reports* 2017 Dec;7(1):16792.
- [4] Falavarjani KG, Mirshahi R, Riazi-Esfahani H, Anvari P, Habibi A, Ashraf Khorasani M, et al. Spatial distribution of diabetic capillary non-perfusion. *Microcirculation* 2021 Jul;28(7):e12719.
- [5] Wong TY, Klein R, Klein BEK, Tielsch JM, Hubbard L, Nieto FJ. Retinal Microvascular Abnormalities and their Relationship with Hypertension, Cardiovascular Disease, and Mortality. *Survey of Ophthalmology* 2001 Jul;46(1):59–80.
- [6] Wong TY, Kamineni A, Klein R, Sharrett AR, Klein BE, Siscovick DS, et al. Quantitative Retinal Venular Caliber and Risk of Cardiovascular Disease in Older Persons: The Cardiovascular Health Study. *Archives of Internal Medicine* 2006 Nov;166(21):2388–2394.
- [7] Engelgau MM, Geiss LS, Saaddine JB, Boyle JP, Benjamin SM, Gregg EW, et al. The Evolving Diabetes Burden in the United States. *Annals of Internal Medicine* 2004 Jun;140(11):945–950.
- [8] Tapp RJ, Shaw JE, Harper CA, Courten MPd, Balkau B, McCarty DJ, et al. The Prevalence of and Factors Associated With Diabetic Retinopathy in the Australian Population. *Diabetes Care* 2003 Jun;26(6):1731–1737.
- [9] Kalogeropoulos D, Kalogeropoulos C, Stefaniotou M, Neofytou M. The role of tele-ophthalmology in diabetic retinopathy screening. *Journal of Optometry* 2020 Oct;13(4):262–268.
- [10] Wu L, Fernandez-Loaiza P, Sauma J, Hernandez-Bogantes E, Masis M. Classification of diabetic retinopathy and diabetic macular edema. *World Journal of Diabetes* 2013 Dec;4(6):290–294.
- [11] Ogurtsova K, da Rocha Fernandes JD, Huang Y, Linnenkamp U, Guariguata L, Cho NH, et al. IDF Diabetes Atlas: Global estimates for the prevalence of diabetes for 2015 and 2040. *Diabetes Research and Clinical Practice* 2017 Jun;128:40–50.
- [12] Popovic N, Lipovac M, Radunovic M, Ugarte J, Isusquiza E, Beristain A, et al. Fractal characterization of retinal microvascular network morphology during diabetic retinopathy progression. *Microcirculation* 2019;26(4):e12531.
- [13] Kauppi T, Kalesnykiene V, Kamarainen JK, Lensu L, Sorri I, Raninen A, et al. DIARETDB1 diabetic retinopathy database and evaluation protocol. In: *Proceedings of the British Machine Vision Conference 2007*; 2007. p. 18.
- [14] Cheung N, Donaghue KC, Liew G, Rogers SL, Wang JJ, Lim SW, et al. Quantitative Assessment of Early Diabetic Retinopathy Using Fractal Analysis. *Diabetes Care* 2009 Jan;32(1):106–110.
- [15] Lim SW, Cheung N, Wang JJ, Donaghue KC, Liew G, Islam FMA, et al. Retinal Vascular Fractal Dimension and Risk of Early Diabetic Retinopathy: A prospective study of children and adolescents with type 1 diabetes. *Diabetes Care* 2009 Nov;32(11):2081–2083.
- [16] Broe R, Rasmussen ML, Frydkjaer-Olsen U, Olsen BS, Mortensen HB, Hodgson L, et al. Retinal Vessel Calibers Predict Long-term Microvascular Complications in Type 1 Diabetes: The Danish Cohort of Pediatric Diabetes 1987 (DCPD1987). *Diabetes* 2014 Nov;63(11):3906–3914.
- [17] Broe R, Rasmussen ML, Frydkjaer-Olsen U, Olsen BS, Mortensen HB, Peto T, et al. Retinal vascular fractals predict long-term microvascular complications in type 1 diabetes mellitus: the Danish Cohort of Pediatric Diabetes 1987 (DCPD1987). *Diabetologia* 2014 Oct;57(10):2215–2221.
- [18] Broe R. Early risk stratification in paediatric type 1 diabetes. *Acta Ophthalmologica* 2015;93(A102):1–19.
- [19] Carlsson G. Topology and data. *Bulletin of the American Mathematical Society* 2009;46(2):255–308.
- [20] Otter N, Porter MA, Tillmann U, Grindrod P, Harrington HA. A roadmap for the computation of persistent homology. *European Physical Journal – Data Science* 2017;6(17):1–38.
- [21] Ghrist R. Barcodes: The persistent topology of data. *Bulletin of the American Mathematical Society* 2008;45(1):61–75.

- [22] Cohen-Steiner D, Edelsbrunner H, Harer J. Stability of Persistence Diagrams. *Discrete & Computational Geometry* 2007 Jan;37(1):103–120.
- [23] Koseki K, Kawasaki H, Atsugi T, Nakanishi M, Mizuno M, Naru E, et al. Assessment of skin barrier function using skin images with topological data analysis. *npj Systems Biology and Applications* 2020 Dec;6(1):1–9.
- [24] Nicolau M, Levine AJ, Carlsson G. Topology based data analysis identifies a subgroup of breast cancers with a unique mutational profile and excellent survival. *Proceedings of the National Academy of Sciences* 2011 Apr;108(17):7265–7270.
- [25] Belchi F, Pirashvili M, Conway J, Bennett M, Djukanovic R, Brodzki J. Lung Topology Characteristics in patients with Chronic Obstructive Pulmonary Disease. *Scientific Reports* 2018 Dec;8(1):5341.
- [26] Aljanobi FA, Lee J. Topological Data Analysis for Classification of Heart Disease Data. In: *2021 IEEE International Conference on Big Data and Smart Computing (BigComp)*; 2021. p. 210–213. ISSN: 2375-9356.
- [27] Hajj M, Zamzmi G, Batayneh F. TDA-Net: Fusion of Persistent Homology and Deep Learning Features for COVID-19 Detection in Chest X-Ray Images. *arXiv:210108398 [cs, eess]* 2021 Aug;.
- [28] Hickok A, Needell D, Porter MA. Analysis of Spatiotemporal Anomalies Using Persistent Homology: Case Studies with COVID-19 Data. *arXiv:210709188 [physics, q-bio]* 2021 Jul;.
- [29] Singh G, Mémoli F, Carlsson G. Topological Methods for the Analysis of High Dimensional Data Sets and 3D Object Recognition. *Eurographics Symposium on Point-Based Graphics* 2007;p. 10.
- [30] Bendich P, Marron JS, Miller E, Pieloch A, Skwerer S. Persistent Homology Analysis of Brain Artery Trees. *The Annals of Applied Statistics* 2016;10(1):198–218.
- [31] Stolz BJ, Kaeppler J, Markelc B, Mech F, Lipsmeier F, Muschel RJ, et al. Multiscale Topology Characterises Dynamic Tumour Vascular Networks. *arXiv:200808667 [math, q-bio]* 2020 Aug;.
- [32] Nardini JT, Stolz BJ, Flores KB, Harrington HA, Byrne HM. Topological data analysis distinguishes parameter regimes in the Anderson-Chaplain model of angiogenesis. *PLOS Computational Biology* 2021 Jun;17(6):e1009094.
- [33] Garside K, Henderson R, Makarenko I, Masoller C. Topological data analysis of high resolution diabetic retinopathy images. *PLOS ONE* 2019 May;14(5):e0217413.
- [34] Hoover AD, Kouznetsova V, Goldbaum M. Locating blood vessels in retinal images by piecewise threshold probing of a matched filter response. *IEEE Transactions on Medical Imaging* 2000 Mar;19(3):203–210.
- [35] Staal J, Abramoff MD, Niemeijer M, Viergever MA, van Ginneken B. Ridge-based vessel segmentation in color images of the retina. *IEEE Transactions on Medical Imaging* 2004 Apr;23(4):501–509.
- [36] Fraz MM, Remagnino P, Hoppe A, Uyyanovvara B, Rudnicka AR, Owen CG, et al. An Ensemble Classification-Based Approach Applied to Retinal Blood Vessel Segmentation. *IEEE Transactions on Biomedical Engineering* 2012 Sep;59(9):2538–2548.
- [37] Budai A, Bock R, Maier A, Hornegger J, Michelson G. Robust Vessel Segmentation in Fundus Images. *International Journal of Biomedical Imaging* 2013 Dec;2013:e154860.
- [38] Dirnberger M, Kehl T, Neumann A. NEFI: Network Extraction From Images. *Scientific Reports* 2015;5:15669.
- [39] Schleicher D. Hausdorff Dimension, Its Properties, and Its Surprises. *The American Mathematical Monthly* 2007 Jun;114(6):509–528.
- [40] Adams H, Emerson T, Kirby M, Neville R, Peterson C, Shipman P, et al. Persistence images: a stable vector representation of persistent homology. *Journal of Machine Learning Research* 2017 Jan;18(1):218–252.
- [41] Bhaskara A, Vadgama S, Xu H. Greedy Sampling for Approximate Clustering in the Presence of Outliers. In: *Advances in Neural Information Processing Systems*, vol. 32 Curran Associates, Inc.; 2019. .
- [42] Edelsbrunner H, Harer JL. Persistent homology – A survey. *Contemporary Mathematics* 2008;453:257–282.
- [43] Edelsbrunner H, Harer JL. *Computational Topology: An Introduction*. Providence R. I.: American Mathematical Society; 2010.
- [44] Thorne T, Kirk PDW, Harrington HA. Topological Approximate Bayesian Computation for Parameter Inference of an Angiogenesis Model. *arXiv:210811640 [q-bio, stat]* 2021 Nov;.

- [45] Vipond O, Bull JA, Macklin PS, Tillmann U, Pugh CW, Byrne HM, et al. Multiparameter persistent homology landscapes identify immune cell spatial patterns in tumors. *Proceedings of the National Academy of Sciences* 2021 Oct;118(41).
- [46] Wang F, Casalino LP, Khullar D. Deep Learning in Medicine—Promise, Progress, and Challenges. *JAMA Internal Medicine* 2019 Mar;179(3):293–294.
- [47] Li YH, Yeh NN, Chen SJ, Chung YC. Computer-Assisted Diagnosis for Diabetic Retinopathy Based on Fundus Images Using Deep Convolutional Neural Network. *Mobile Information Systems* 2019 Jan;2019:e6142839.
- [48] Abdelsalam MM. Effective blood vessels reconstruction methodology for early detection and classification of diabetic retinopathy using OCTA images by artificial neural network. *Informatics in Medicine Unlocked* 2020 Jan;20:100390.
- [49] Zhao H, Sun Y, Li H. Retinal vascular junction detection and classification via deep neural networks. *Computer Methods and Programs in Biomedicine* 2020 Jan;183:105096.
- [50] Ching T, Himmelstein DS, Beaulieu-Jones BK, Kalinin AA, Do BT, Way GP, et al. Opportunities and obstacles for deep learning in biology and medicine. *Journal of the Royal Society: Interface* 2018 Apr;15(141):20170387.
- [51] Fu X, Gens JS, Glazier JA, Burns SA, Gast TJ. Progression of Diabetic Capillary Occlusion: A Model. *PLOS Computational Biology* 2016 Jun;12(6):e1004932.
- [52] Alom MZ, Hasan M, Yakopcic C, Taha TM, Asari VK. Recurrent Residual Convolutional Neural Network based on U-Net (R2U-Net) for Medical Image Segmentation. *arXiv:180206955 [cs]* 2018 May;.
- [53] Li M, Chen Y, Ji Z, Xie K, Yuan S, Chen Q, et al. Image Projection Network: 3D to 2D Image Segmentation in OCTA Images. *IEEE Transactions on Medical Imaging* 2020 Nov;39(11):3343–3354.